[Mansoura Engineering Journal](https://mej.researchcommons.org/home)

Volume 27 | Issue 4 Article 11

1-25-2021

3D Numerical and Experimental Analysis of Turbulence Energy Spectrum in Swirl Jet.

Nabil Mostafa
Mechanical Power Department, College of Engineering Zagazig University, Zagazig, 44519, Egypt., mmostafa@egyptnetwork.com

Recommended Citation

Mostafa, Nabil (2021) "3D Numerical and Experimental Analysis of Turbulence Energy Spectrum in Swirl Jet.," *Mansoura Engineering Journal*: Vol. 27 : Iss. 4 , Article 11.
Available at: https://doi.org/10.21608/bfemu.2021.143047

Mansoura Engineering Journal, (MEJ), Vol. 27, No. 4, December 2002. M. 1

3D NUMERICAL AND EXPERIMENTAL ANALYSIS OF TURBULENCE ENERGY SPECTRUM IN SWIRL JET

التحليل الحسابى و التجريبى ثلاثى الأبعاد لطيف الطاقه الاضطرابى فى نفث حلزونى

Nabil H. Mostafa
Mechanical Power Department, College of Engineering
Zagazig University, Zagazig, 44519, Egypt.
E-mail: nmostafa@egyptnetwork.com

خلاصه

تم إجراء التجارب العمليه و الحل العددى لنفث مضطرب يتعرض للإثاره عن طريق حقن نفاثات مولده للدوامات وضعت قرب مخرج المنفث الرئيسى لتوليد نفث حلزونى. وكان رقم رينولدز ١١٣٠٠ للمنفث الرئيسى و كانت نسبه كميه التحرك بين النفاثات المولده للدوامات و النفث الرئيسى ٥,٥ و ٨,٧ %. وكان حقن النفاثات المولده للدوامات يتم مماسيا و مائلا بزاويه ٤٥ و ٩٠ درجه.

إن ديناميكيه انتشار النفث الحلزونى حسبت باستعمال برنامج حسابى لحل معادلات نافير استوكس فى الإتجاهات الثلاثه، حيث يتم تمثيل المعادلات الحاكمه على شبكه منشأه باستخدام نظام فرق الاختلاف المضاد للاتجاه.إن الشبكه المنشأه قد بنيت فى ثلاث اتجاهات مماثله للتركيب الحقيقى لمنفث النفث الحلزونى.إن استعمال نظام البناء الشبكى متعدد الأجزاء والتداخل الاختيارى ساعد فى بناء شبكه من متوازى المستطيلات لاجسام الحاقنات فى تداخلها مع المنفث الرئيسى و مع اختلاف زوايا الحقن. تم الحصول معمليا على متجهات السرعات و طاقه الإضطراب الحركيه باستخدام مجس قياس سرعات ذو أربعة أسلاك ساخنه. و كذلك تم استخدام التحليل الموجى لدراسة محتوى الطاقة الداخلية و المصاحب.

أوضحت النتائج النظريه و العمليه أن الحقن يقسم الطبقات السطحيه داخل النفث لعدد من الأجزاء مساوى لعدد المحاقن. و فى داخل كل جزء دوامه تنمو عند خروجها من المنفث فى المنطقه الحره. إن استخدام النفاثات المولده للدوامات يزيد زاويه انتشار النفث عن حاله النفث غير المثار. كما إن النفث الحلزونى لديه طاقه حركيه للإضطراب أعلى من النفث غير المثار. أن النفث الحلزونى ذو الحقن المماسى مع أعلى نسبه كميه تحرك يعطى أعلى طاقه حركيه للإضطراب مقارنتا بالنفث غير المثار. و لقد وجد أن النفث الحلزونى يعطى طاقه حركيه للإضطراب مرتفعه فى منطقه اسطوانيه عند قطر يساوى ٨ر. من قطر المنفث وعلى ارتفاع يقدر من ٢ الى ٣ أقطار المنفث متوقفا على نسبه الاندفاع. إن التحليل الموجى اثبت أن النفث الحلزونى المماسى لديه التاثير القوى فى زياده طاقه الاضطراب الحركيه على الطبقات السطحيه للنفث بينما النفث الحلزونى ذو الحقن بزاويه ٤٥° لديه طاقه أكبر فى منطقه المحور الرئيسى. وإنه في منطقة نهاية المريان و على بعد يساوى ثلاث أمثال قطر المنفث فان عدد الموجات و طاقاتها تنتشر على نطاق واسع من الترددات و أعداد الموجات. و هذا يوضح أن إستعمال النفاثات المولدة للدوامات في المنفث الرئيسي يؤدى إلى نطاق واسع من الاضطراب المريانى الذى يؤثر على تذبذب المرعات و يدعم الخلط بين النفث المضطرب و المائع المحيط. أوضحت النتائج اتفاقا جيدا بين النتائج العمليه و النظريه.

Abstract

An experimental analysis and numerical computation of a turbulent jet subjected to Vortex Generating Jets, VGJ, placed at the exit of the main jet nozzle to generate swirl jet were conducted. The main jet had a R_{en} about 11300, and the VGJ to main jet momentum ratio were 0.055 or 0 078. The activation of VGJ was tangential ($\alpha=0°$), ($\alpha=45°$) and ($\alpha=90°$).

In Swirl Jets, the dynamics of the flow field structure were computed using a three-dimensional Navier-Stokes code. The governing equations are discretized on 3D structured grid using an upwind difference scheme. The grid was build as 3D geometry and similar to swirl jet real nozzle. The use of the multiblock structured grid system and the arbitrary interfaces between the VGJs hexahedral grids and main jet hexahedral grids facilitate building a real 3D swirl jet grid geometry with changing injection angle. The macroscopic behavior of the jet evolution is discussed with the turbulence kinetic energy and its dissipation rate The experimental velocity vectors and Total Turbulent Kinetic Energy, TTKE, contours obtained with a four-wire hot-wire velocity probe The wavelet energy density is used to measure the intermittency and associated energy content

---

Accepted November 9, 2002.

The theoretical and experimental results show that the injection deviates the boundary layer flow inside the nozzle into a number of sections equal to the number of VGJs. Each section characterized by its own vortex. The vortices, which are generated from VGJs inside the nozzle tube, are growing outside the nozzle at the free zone. VGJs enhance the jet-spreading angle over unexcited jet. The swirl jet has higher TTKE, than the baseline jet. The VGJs increased and spreaded the turbulent kinetic energy in the main (swirl) jet. The swirl jet with tangential injection and higher momentum injection ratio ($\alpha = 0$, mr = 0.078) gives the highest TTKE. For swirl jet the higher TTKE region is located at a cylinder layer of diameter 0.8 of nozzle diameter and moving horizontally in a section from Z/D=2 to Z/D=3 according to momentum ratio. Wavelete analysis presents that tangential swirl jet have a stronger effect on increasing the turbulent kinetic energy at the jet border, while, swirl jet at α=45° has higher power level at axial location. Further downstream, the total wavenumber energy is distributed to a wide range of frequencies and wavenumbers. This indicates that a wide range of turbulence structures associated with the VGJs injection affects the velocity fluctuations and enhances mixing between turbulent jet and surrounding fluid. There is a good matching between the experimental and computational results.

Keywords
Swirl Jet, Vortex Generating Jets, CFD, Turbulent, and Wavelet analysis.

NOMENCLATURE

C_{jet}	mean velocity of main jet (m/s).
C_{vgj}	mean velocity of VGJ jet (m/s).
$C_{\mu}, C_{\varepsilon}, C_K$	constants.
d_{vgj}	diameter of the VGJ nozzle (mm).
D or d_{jet}	diameter of main jet nozzle (mm).
f	frequency.
mr	momentum ratio of the flow of the VGJs to the main jet flow momentum.
r, t	local polar, radial and tangential coordinates, respectively.
r_o, t_o	main polar, radial and tangential, coordinates, respectively.
R_{en}	Reynolds' number.
U	axial velocity, (m/s).
u	turbulence fluctuation component of axial velocity, (m/s).
V	horizontal velocity component in r-axis, (m/s).
v	turbulence fluctuation component of V velocity, (m/s).
VR	ratio of the VGJ velocity to the main jet velocity.
W	the horizontal velocity component in the direction of t_o-axis, (m/s).
Wn	wave number, (rad/cm).
w	turbulence fluctuation component of W velocity, (m/s).
z	axial coordinate.

GREEK LETTERS

α	angle of VGJ injector axis relative to tangent of nozzle cross section in degrees.
β	angle between VGJ axis and main jet axis in degrees.
ε	turbulence dissipation rate, (J/kg s).
κ	turbulence kinetic energy, (m^2/s^2).
ν_t	turbulent viscosity, (m^2/s).
θ	jet total spreading angle in degrees.
ρ	density, (kg/m^3).

$\sigma_k, \sigma_\varepsilon$ constants.

μ dynamic viscosity, (pa.s).

Δx distance

SUFFIXES

jet	main jet.
vgj	vortex generating jet.

ABBREVIATIONS

PSJ	Pulsed Swirl Jet generated from the interaction between pulsed injections of VGJs with a free jet.
SJ	Swirl Jet generated from the interaction between continuous injections of VGJs with a free jet.
TTKE	Total Turbulent Kinetic Energy, $(\overline{u}^2 + \overline{v}^2 + \overline{w}^2)/2$.
VGJ	Vortex Generating Jet.

1- INTRODUCTION

Many fossil fuel burning power plants and industrial combustors are subject to ever increasingly stringent regulation of allowed emissions levels. Thus it is highly desirable to control the emissions levels through direct control of the combustion process. Swirl Jet is an example of applications where attempting use of fully premixed reactants. In these cases it is still desirable to reduce the levels of pollutants generation from the levels of a diffusion flame. This should be achievable by enhancing the mixing between the entrant fuel charge and the air stream with controlling jet evolution.

Controlling the jet evolution can be obtained by passive and active methods. Passive methods are limited for certain performance like using vortex ring, which was analyzed, by Martin and Meiburg (1991). Also, using small tabs at nozzle exit, Zaman et al., (1994), or crown shaped nozzles, which was limited by the number and length of the crown teeth, Longmire et al (1992). Corke and Kusek (1993) discussed active control of fundamental two-and three dimensional amplified modes in an axisymmetric jet by introducing localized acoustic disturbances produced by an azimuthal array of miniature speakers placed close to the jet lip on the exit face. Husain and Hussain (1993) discussed the dynamics of the preferred mode coherent structure in the near field of elliptic jets. They also addressed the effect of initial conditions and excitation frequency and amplitude on the elliptic jet instability and its evolution.

Although convenient and easy to use, acoustic drivers are mostly not suitable for controlling flows of practical interest. Among the many reasons, which can be cited, are lack of space for installation, loss of effectiveness in noisy environments like combustors and possible reliability problems. Alternative active methods have been also examined, these included mainly mechanically vibrating elements at the jet exit. Piezoelectric actuators were used to excite free shear flows for square jet by Wiltse and Glezer (1993). Vandsburger and Ding (1995) examined a triangular nozzle fitted with mechanically amplified piezoceramic actuators on all three sides. For the purpose of achieving control over the jet evolution into the far field (L/D = 30) various azimulthal (spatial) modes were excited. It was found that fractional spatial modes and wave combinations offered the best jet mixing control.

In spite of the wealth of data available, industry shies away from using moving parts as flow actuators. Therefore, a practical excitation device should have minimum power consumption and no moving parts, while producing an excitation that is controllable in frequency, amplitude and phase. The possibility exists for employing fluid jet actuators. The viability and performance of an unsteady fluid-dynamic excitation system was examined by Raman and Cornelius (1995) for the control of turbulent jets. They demonstrated that a jet flow could be forced by two miniature fluidic exciter jets.

This technique produced very large velocity perturbations in the main jet. The application of fluid based actuators to subsonic jets has been examined in recent years by the group of Glezer at Georgia Tech using "synthetic jets" (Parekh et al 1996). These actuators add no mass, but do add momentum for actuation to the excited jet.

The evolution of a free round jet using vortex generating jets placed around the main jet nozzle exit (named Swirl Jet) was presented by the author previously, Mostafa et al. (1995). Activation of the VGJs resulted in enhanced mixing of the jet fluid and the ambient fluid. The activation of tangential (α=0) VGJs in a pulsed manner enhanced the main jet spreading over continuous VGJs, Mostafa et al. (1996).

Flow in free shear flows like jets and mixing layers are characterized by vortex formation. In these regions, the turbulence intensity is very high. These structures play cruciral rule in controlling the mixing between two fluid streams. Turbulence scales results from strong pressure fluctuations on the mixing layer or the jet exit. Time domain analysis such as conditional sampling has been used to characterize significant velocity or pressure fluctuation and related that to fluid flow phenomena. Frequency domain analysis has been used to characterize the energy distribution among the frequency components. Correlation functions in frequency and time domains have also been used to statistically describe wall pressure fluctuations Beall et al. (1982). The interest in time/space and spatial characterization of pressure fluctuations stems from the interest in problems where flow-induced vibrations and or sound generation are important. Such characteristics, represented in terms of a wavenumber-frequency spectrum, would serve as an input to determine the response of structures or noise generation levels.

The objective of this paper is to study the flowfield turbulence energy and evolution in a swirl jet, "a free jet subjected to excitation of VGJs" experimentally and numerically. Specifically the turbulent kinetic energy is determined from measurements of u, v, and w with examining the energy contents of the vortices by wavelet analysis technique. The dynamics of the flow field structure of swirl jets are computed using a three-dimensional Navier-Stokes code with upwind difference scheme. The grid is build as real 3D swirl jet geometry. The macroscopic behavior of the jet evolution is discussed with the turbulence kinetic energy and its dissipation rate. The main parameters of the study are the angle of the VGJs with respect to the main jet, and the momentum ratio between the VGJs and the main jet. The transport of swirl jet fluid is compared with the unexcited jet.

2- THEORY BACKGROUND

The basic approach is to use standard viscous flow (Navier- Stokes) equations with provisions for variable density and a conventional turbulence model, such as κ-ε, model. A numerical model previously developed by CFDRC to solve (Navier- Stokes) equations (Sighal 1999). The issue of turbulence modeling arises from the need to represent turbulent or Reynolds stresses, which are additional unknowns introduced by time averaging the Navier- Stokes equations. One common approach is the Eddy Viscosity Modeling (EVM) in which the Reynolds stress tensor is assumed to be proportional to the rate of mean strain, by analogy with the laminar stress- strain relationship. The proportionality parameter is called the turbulent or eddy viscosity. Unlike its laminar counter- part, the turbulent viscosity is not a property of the fluid but rather a characteristic of the flow. Several versions of the κ-ε model are in use in the literature. They all involve solutions of transport equations for turbulent kinetic energy (κ) and its rate of dissipation (ε). In the model, the turbulent viscosity is expressed as,

$$\nu_t = \frac{C_\mu . k^2}{\varepsilon} \qquad (1)$$

The transport equations for k and ε are,

$$\frac{\partial}{\partial t}(\rho.k)+\frac{\partial}{\partial x_j}(\rho u_j.k)=\rho.P-\rho.\varepsilon+\frac{\partial}{\partial x_j}[(\mu+\frac{\mu_t}{\sigma_k})\frac{\partial k}{\partial x_j}] \quad (2)$$

$$\frac{\partial}{\partial t}(\rho.\varepsilon)+\frac{\partial}{\partial x_j}(\rho.u_j.\varepsilon)=C_{\varepsilon 1}\frac{\rho.P.\varepsilon}{k}-C_{\varepsilon 1}\frac{\rho.\varepsilon^2}{k}+\frac{\partial}{\partial x_j}[(\mu+\frac{\mu_t}{\sigma_\varepsilon})\frac{\partial \varepsilon}{\partial x_j}] \quad (3)$$

where the product term P is defined as

$$P=\nu_t(\frac{\partial u_i}{\partial x_j}+\frac{\partial u_i}{\partial x_j}-\frac{2}{3}\frac{\partial u_m}{\partial x_m}\delta_{ij})\frac{\partial u_i}{\partial x_j}-\frac{2}{3}k\frac{\partial u_m}{\partial x_m} \quad (4)$$

3- GRID STRUCTURE AND BOUNDARY CONDITIONS

The swirl jet flow analysis is computed for different momentum ratio of the VGJ flow to main jet flow. There are four sets of results that are computed for unexcited jet (baseline jet) and swirl jet at different injection angles (α=0°, 45, 90°). The swirl jet grids structure is shown in Fig. 2a. This uses the multiblock system. The structure grids are divided into five blocks in the nozzle each have at least 21x16x15, nine blocks downstream 21x11x21 grid points and four blocks for the VGJ's 5x5x10 as shown in Figs. 2b and 2d. The grids are clustered near the VGJ to solve the fluid interaction. There are arbitrary interfaces between the VGJ's hexahedral grids and main jet hexahedral grids. The length of the grid in physical domain is about 56 d_{jet} length and 47 d_{jet} diameter as shown in Figs. 2b and 2c.

The upstream boundary conditions are 10 m/s axial velocity, 174 N/m^2 gauge pressure, turbulence kinetic energy (κ=0.01 m^2/s^2) and turbulence dissipation rate (ε=10 0 J/kg.s). The downstream boundary conditions are atmospheric pressure, turbulence kinetic energy (κ=0.0 m^2/s^2) and turbulence dissipation rate (ε=0.0 J/kg.s). The momentum ratio of the flow of the VGJs to the main jet flow momentum is (0.055 and 0.078). Fluids in all blocks are completely air and the temperature is constant at 300 K.

4. EXPERIMENTAL FACILITY, METHODS AND PARAMETERS

The experiments were carried out in a small jet facility at the Reacting Flows Laboratory of the Mechanical Engineering Department at Virginia Tech. The flow rate of the main jet and the VGJs were kept constant. Air, at room temperature, issued from a 17 mm round nozzle at a Reynolds number of 11,300. The velocity ratio between the VGJs and main jet (VR=Cj/Cm) was set to unity and 1.41 resulting in a VGJ to main jet momentum ratio of 0.055 and 0.078. A schematic of the jet construction is shown in Fig 1. Note that the jet actually issued out of a tube with a wall thickness of 0 9 mm thus no back step was present. The four VGJs had a 2 mm inside diameter. The injection angle (α) of the VGJs with respect to a tangent to the main nozzle, was set to α=0° and 45°.

The jet flowfield was investigated at axial locations from z/D = 0 to z/D = 20 (0.01 mm to 340 mm) Within that region, four different measuring grids spacing were used. The first grid region had 7 circular horizontal levels, starting from Z/D= 0 006 to Z/D=3 in 0.5 diameter steps. Each consecutive level's diameter increased by 0.12 jet diameters. Grid points were spaced every r_o/D= 0 06 (1 mm). The second grid region spanned from Z/D= 3 to Z/D = 7 The third region spanned from Z/D=7 to Z/D=14, and the last region spanned from Z/D=14 to Z/D=20 In the last three regions the horizontal measuring planes were spaced every one diameter downstream. Also, regions grid spacing was set at 1, 2 and 4 mm in the second, third and fourth regions respectively. Thus, the entire sampling region contained 18187 nodes where three velocity components and their rate of change were measured

A four-wire hot-wire anomemeter probe (AVOP-4-100) manufactured by Auspex Corporation, USA, was used to measure the local three velocity components. The sensors are arranged to form two orthogonal "x" wire arrays. The wire sensors are 5 µm diameter tungsten of 1.1 mm length, oriented nominally 45° to the probe axis. At each probe location, 1008 samples of hot-wire voltages were collected. Samples were collected simultaneously on four channels (one for each wire) using a DT 2838 A/D board at approximately 8 kHz per channel. Each anemometer channel was equipped with an anti-aliasing low-pass filter set at 3.8kHz. Three-component velocity information was calculated from the raw voltage data using the method of Wittmer et al. (1998). For wavelet analysis each location was acquired thirty times of data consecutively.

5- METHODS OF EXPEREMENTAL DATA ANALYSIS

The wavenumber frequency spectrum is estimated using the technique introduced by Beall et al. (1982). The technique uses measurements of a fluctuation field such as pressure or velocity at two locations separated by a distance Δx. The measurements are divided into time segments each consisting of N samples. From either of the two records, the auto-power spectrum is computed which provides an estimate of the power associated with a frequency interval f_i and $f_i+\Delta f_i$. Using the two records, the cross-power spectrum is computed. From the phase of the cross-power spectrum $\theta_i(f_i)$, the local wavenumber $Wn_i(f_i) = \theta_i(f_i)/ \Delta x$ is determined. This wavenumber is called local because it is estimated over the separation Δx and is different from wavenumbers obtained by applying a spatial Fourier transform to measurement from many spatial locations. The local wavenumber gives a better estimate of spatial characteristics in a spatially varying field. Having the frequency f_i and an associated local wavenumber, Wn_i, the amount of power, $S(f_i)$, is recorded at the co-ordinate point (f_i, Wn_i) in the wavenumber frequency, f-Wn plane. Because, there is a stochastic relationship between wavenumber and frequency, every segment may yield different estimates of the power $S(f_i)$ and wavenumber $Wn_i(f_i)$ for the frequency interval f_i and $f_i+\Delta f$. The new level of power is entered at a new co-ordinate point consisting of the new value of Wn_i. This process is repeated for all data intervals to obtain the average power, $S_l\ (Wn_i,\ f_i)$, associated with every frequency and every wavenumber in the wavenumber frequency plane. This power is an estimate of the local wavenumber frequency spectrum. The limits of the measured wavenumbers and the resolution are determined by the separation distance between the pressure taps, Δx and the number of grid elements in the wavenumber-frequency domain. The wavenumber that can be obtained are bounded by $-\pi/ \Delta x$ and $\pi/\Delta x$. The wavenumber resolution can be adjusted by setting the number of cells, which in all of our analysis was set at 256.

From the local wavenumber frequency spectrum $S_l\ (Wn_i,\ f_i)$, the frequency spectrum $S_i(f_i)$ can be estimated by integrating the spectrum over all wavenumbers, i.e.

$$S_l(f_i) = \Sigma_k\, S_l\,(Wn_i,\ f_i) \tag{5}$$

and the local wavenumber spectrum $S_l(Wn)$ can be estimated by integrating the spectrum over all frequencies, i.e.

$$S_l(Wn) = \Sigma_f\, S_l\,(Wn_i,\ f_i) \tag{6}$$

The results presented here were obtained from 30 data segments; each segment containing 128 data points and sampled at 125 Hz. This yielded a Nyquist frequency of 62.5 Hz with a frequency resolution of 0.98 Hz. Depending on the measuring location, the separation Δx was set at 1 mm.

6. RESULTS AND DISCUSSION

The main jet structure and evolution, baseline and excited swirl jet, was studied experimentally and numerically via three component velocity and turbulence intensity maps. The data are presented as vectors and iso-value contours. The Swirl Jet flow analysis is computed for different momentum ratio of the VGJ flow to main jet flow. There are four sets of results that are computed for unexcited jet (baseline jet) and Swirl Jet at different injection angles ($\alpha=0^\circ$, 45°, 90°).

6.1- Mean Flow Analysis

Mean velocity components (U, V, W) for the baseline jet and a jet subjected to VGJs at momentum ratio (0.055 and 0.078) and injection angles 0°, 45° and 90° were studied

A comparison of the theoretical velocity vector projection at the horizontal injection plane (i.e. the resultant of radial and normal velocities) for the above seven conditions is shown in Fig. 3 The injection deviated the boundary layer flow inside the nozzle into four sections especially at injection angles 0° and 45°. The effect of ninety degree injection is only concentrated at the front of the VGJs. Each section characterized by its own vortex. The higher VGJs momentum case mr=0.078 exhibits higher horizontal velocity component than baseline jet and swirl jet with lower momentum ratio cases mr=0 055.

A comparison between the theoretical and experimental velocity vector projection on horizontal plane at the jet exit (Z/D=0) for the baseline jet and a jet subjected to VGJs at momentum ratio (0.055 and 0.078) and injection angles 0° and 45° are shown in Figs. 4 and 5 respectively. The mean flow is defined experimentally by a simple average over 1008 samples at each measuring point. The plots of Figs. 4 and 5 clearly show the formation of four of vortices at the jet exit as a result of the VGJs activation. The four vortices, which generated from VGJs inside the nozzle tube (demonstrated in Fig. 3) are grown outside the nozzle. The higher VGJs momentum case mr=0.078 exhibits higher horizontal velocity component than baseline jet and swirl jet with lower momentum ratio cases mr=0.055. From the shown results it is clear that experimental results matched with the theoretical results.

6.2: Turbulent Kinetic Energy

A primary objective of this paper is to study the turbulence production mechanisms in the swirl jet. The turbulence characteristics of the baseline and excited jets were obtained from the hot wire data and are presented in the form of the total turbulent kinetic energy $[(\overline{u}^2+\overline{v}^2+\overline{w}^2)/2]$. The turbulence characteristics are also computed numerically as turbulent kinetic energy (κ) and its rate of dissipation (ε). The data are presented in the form of iso-contours at different horizontal planes and a vertical diametric plane.

Isovalue contour plots of numerical turbulent dissipation rate (ε) in a horizontal plane at jet exit (Z/D=0) are shown in Fig. 6, for the baseline jet and a jet subjected to VGJs at momentum ratio 0.055 and 0.078 and injection angles of 0°, 45° and 90°. The maximum value of (ε) in the above seven conditions are at the tangential injection of VGJs. The swirl jet with 45° is also higher than baseline jet. The increases of maximum turbulent dissipation rate contours in the swirl jet are concentrated near the injection ports of VGJs.

The swirl jet numerical turbulent kinetic energy, (κ), map are presented into two dimensional iso-value contour. Horizontal contour map at (Z/D=0) of the turbulent kinetic energy for the baseline jet and a jet subjected to VGJ at (α=0°, mr=0.055), (α=45°, mr=0.055), (α=0°, mr=0 078), and (α=45°, mr=0.078) are shown in Figs. 7.A1 to 7.A5, respectively. All VGJs excited cases show higher turbulent kinetic energy than the baseline jet. The higher VGJs momentum case, mr=0.078, exhibits higher turbulent kinetic energy than the case of mr=0.055 The tangential VGJs momentum exhibits higher turbulent kinematics energy than the case of α=45°. With the excitation the high stress region located near the injection ports of VGJs. As a comparison with experimental TTKE data, using hot wire probe, at horizontal section, Z/D = 0, are shown in Fig 8 The maximum TTKE in the above five conditions are 1 27, 3.6, 1.9, 5.1 and 2.6 m^2/s^2 respectively The percentage increase of total turbulence kinetic energy in the swirl jet relative to the baseline jet was calculated to be 183.4, 49.6, 300.1, and 104.7% respectively for the above swirl jet four conditions. The data indicates that the highest turbulent kinetic energy is generated with tangential injection (α = 0) of the VGJs. Of course as the momentum ratio increases so does the turbulent kinetic energy. Matching between the experimental and theoretical results can be noticed.

To follow-up the variation of the turbulence kinetic energy at downstream in the same five previous conditions. the numerical and experimental results at horizontal section, Z/D=3, are plotted in Figs. 9 and 10 respectively. These figures show that the TTKE is increased and spreaded inside the swirl jet structure in the direction of downstream flow. The view of four vortexes still formed at that level. There is complete matching between the experimental and theoretical results. At the level of Z/D=3, the maximum TTKE for all five cases discussed are 1.872, 3.09, 3.08, 3.155 and 3.117 m^2/s^2 respectively as shown in Fig. 10. All VGJs excited cases show higher turbulent kinetic energy than the baseline jet. The higher VGJs momentum case mr=0.078 exhibits higher turbulent kinetic energy than the case mr=0.055 The swirl jet with tangent injection has higher TTKE than injection with 45°

The swirl jet turbulent kinetics energy, (κ), map are presented into two dimensional iso-value contour. Axial contour map of the turbulent kinetic energy for the baseline jet and a jet subjected to VGJs at (α=0°, mr=0.055), (α=45°, mr=0.055), (α=0°, mr=0.078), and (α=45°, mr=0.078) are shown in Fig.11. All VGJs excited cases show higher turbulent kinetic energy than the baseline jet. The higher VGJs momentum case mr=0.078 exhibits higher turbulent kinetic energy than the case mr=0.055. With excitation the high stress region located at a cylinder layer of diameter 0.8 of nozzle diameter and moving horizontally in a section from 2 to 3 z/D from upstream according to momentum ratio.

As a comparison with experimental data using hot wire probe, the swirl jet total turbulent kinetic energy map are presented into two dimensional iso-value contour. Axial contour map of the TTKE for the above five conditions are shown in Fig. 12. All VGJs excited cases show higher turbulent kinetic energy than the baseline jet as the numerical results. The higher VGJs momentum case mr=0.078 exhibits higher turbulent kinetic energy than the case of mr=0.055. Also, as indicated numerically, with swirl jet excitation the high stress region located at a cylinder layer of diameter 0.8 of nozzle diameter and at horizontal section of 2.2 z/D from upstream. Tangential VGJs injection exhibits higher TTKE than others, which is completely matched with the theoretical results.

6-3 Space/time spectrum characteristics of velocity fluctuations

The characteristics of velocity fluctuations in baseline jet and swirl jet have been described in both time and frequency domains. For instance, conditional sampling has been used to identify significant velocity events at each point and to relate such events to velocity characteristics in turbulent boundary layers. Frequency domain analysis has been used to characterize the energy distribution among the frequency components. Correlation functions in frequency and time domains have also been used to describe velocity fluctuations statistically. Such characteristics, represented in terms of a wave number–frequency spectrum, would serve as an input to determine time/space and spatial characterization of velocity fluctuations.

The downstream variation of the frequency power spectrum of the axial jet velocity fluctuations for the baseline jet and a jet subjected to VGJs at (α=0°, mr=0.055) and (α =45°, mr=0.055) at two positions of axial diametric coordinate, (Z/D= 0, r_o/D=0, t_o/D=0) and (Z/D=3, r_o/D=0, t_o/D=0) are shown in Figs. 13.a and 13.b respectively. There are also other two positions at the jet border, (Z/D= 0, r_o/D=0.4, t_o/D=0) and (Z/D=3, r_o/D=0.4, t_o/D=0). Their frequency power spectrum are shown in Figs 13.c and 13.d respectively. Based on the sampling rate of the velocity fluctuations, the highest analyzed frequency component is 62.5 Hz. The lowest component, as determined from the record length, is 0.98 Hz. The frequency spectra shows that, at axial diametric coordinate, the level of energy in all frequency components are varying along the spectrum. The power amplitude of the swirl jet has a higher amplitude than the baseline jet. The level difference of energy between baseline jet and these cases of swirl jet are slightly small at Z/D=0, but this deference is larger than five times at Z/D=3 as shown in Figs 13.a and 13.b. The frequency domain analysis, for the above conditions, indicates that the power of the swirl jet at α =45°, at that axial diametric location, has higher level at 5-20 Hz and 40-55 Hz. But, at the jet border (r/D=0.4) the highest power amplitude is generated from the swirl jet with tangential injection and has higher value at the plane level of Z/D=3. These are around frequency spectrum of 20-30 Hz and 50-60 Hz as shown in Figs. 13.c and 13.d.

The range of wavenumbers *$Wn_i(f_i)$* associated with the frequency f_i components shown in Fig. 13 for the above condition is given in the estimates of the power, $S_l(k_i, f_i)$ at the above four positions shown in Figs. 14, 15, 16 and 17 respectively. Each of them represents baseline jet and swirl jet with injection at (α=0 and 45°). Figures 14 and 15 show that, in all the above cases, the level of energy has different peaks in most frequency components. This means that the energy is divided into small vortices along the frequency spectrum. Further downstream, at z/D=3, the spectral energy of velocity fluctuations is greater than at previous location z/D=0 as shown in Fig. 14. The power level of the swirl jet at α=45°, at that axial location, is higher than the others. Figures 16 and 17 show that, in all the above cases, the level of energy has different peaks in most frequency components at the jet border. This means that the energy is divided into small vortices along the frequency spectrum. Further downstream, at Z/D=3, the spectral energy of velocity fluctuations is greater than at previous location z/D=0 as shown in Fig 16. The power level of the swirl jet with tangential injection (α=0°), at the jet border (r/D=0.4), is higher than the others.

Wave number power spectrum, $S_l(Wn)$, of the velocity fluctuations for the above conditions obtained by integrating the wavenumber frequency spectrum, $S_l(Wn_i, f_i)$, are shown in Figs. 18.a, b, c and d. Figure 18 shows that, in all the above cases, the level of energy has different peaks with wavenumber. The power amplitude of swirl jet has higher amplitude than the baseline jet. The level difference of energy between baseline jet and these cases of swirl jet is slightly small at Z/D=0, but this deference is larger than five times at Z/D=3 as shown in Figs. 18.b and 18 d. At the jet border (r/D=0.4) the highest power amplitude is generated from the swirl jet with tangential injection and has higher value at the plane level of z/D=3 as shown in Figs. 18c and 18.d

7- CONCLUSIONS

The use of vortex generating jets to enhance the mixing between a turbulent jet and the surrounding fluid was shown to offer improvement and control over the jet evolution.

- The injection deviates the boundary layer flow inside the nozzle into a number of sections equals to the number of VGJs. Each section characterized by its own vortex.
- The vortices, which generated from VGJs inside the nozzle tube, are grown outside the nozzle at the free zone.
- The swirl jet has higher total turbulent kinetic energy than the baseline jet. The VGJs increase and spread the turbulent kinetic energy in the main (swirl) jet.
- The swirl jet with tangential injection and higher momentum injection (α = 0, mr = 0 078) gives TTKE higher than the baseline Jet. The percentage increase of total turbulence kinetic energy at exit of the swirl jet relative to the baseline jet, is 183 4, 49.6, 300.1, 104.7 % for swirl jet subjected to VGJs at (α=0°, mr=0.055), (α=45°, mr=0.055), (α=0°, mr=0.078), and (α=45°, mr=0.078) respectively.
- For swirl jet the higher TTKE region is located at a cylinder layer of diameter 0.8 of nozzle diameter and moving horizontally in a section from Z/D=2 to Z/D=3 from upstream according to momentum ratio.
- Tangential VGJs injection have a stronger effect on increasing the turbulent kinetic energy, while, swirl jet at α=45° has higher power level at axial location.
- Further downstream, the total wavenumber energy is distributed to a wide range of frequencies and wavenumbers. This suggests that a wide range of turbulence structures associated with the VGJs injection affects the velocity fluctuations and enhances mixing between turbulent jet and surrounding fluid.

- The using of a three-dimensional Navier-Stokes code with upwind difference scheme and 3D swirl jet grid geometry are completely simulate the macroscopic behavior of the jet evolution with the turbulence kinetic energy and its dissipation rate in the intersection region and the free jet flow.
- The use of the multiblock structured grid system and the arbitrary interfaces between the hexahedral grids of VGJ's and main jet facilitate building a real 3D swirl jet grid geometry with changing injection angle.
- Examining the energy contents of the vortices by wavelet analysis technique compared with the turbulent kinetic energy explain the swirl jet evolution.
- There is good matching between the experimental and theoretical results.

8- REFERENCES

Beall, J.M., Kim,Y C., and Powers, E.J., 1982 "Estimation of Wave Number and Frequency Spectra Using Fixed Probe Pairs," *Journal Applied Physics* Vol. 53, pp.3933-3940.

Corke, T. C. and Kusek S. M., 1993, "Resonance in Axisymmetric Jets With Controlled Helical-Mode Input" *Journal of Fluid Mechanic*, Vol. 249, pp. 307-336.

Husain, H.S. and Hussain, F., 1993, "Elliptic Jets. Part 3. Dynamics of Preferred Mode Coherents Structure", *Journal of Fluid Mechanic*, Vol. 248, PP. 315-361.

Longmire, E. K., Eaton J. K. and Elkins, C. J., 1992, "Control of Jet Structure by Crown-Shaped Nozzles," *AIAA Journal*, Vol. 30, No. 2. pp. 505-512.

Martin, J. E. and Meiburg, E., 1991, "Numerical Investigation of Three-Dimensionally Evolving Jets Subject to Axisymmetric and Azimuthal Perturbations," *J. Fluid Mech.*, Vol 230, pp. 271-318.

Mostafa, N. H., Rediniotis, O.K. and Vandsburger, U., 1995, "Flow Field Characteristics Circular Swirl Jet Generated by Vortex Generating Jets", *ASME Fluids Engineering Division Summer Meeting, High Speed Jet Flows Forum.* PP.89-95. Hilton Head Island, South Carolina.

Mostafa, N. H., Vandsburger, U., and Economides, T.A., 1996, "Flow Field Characteristics of a Turbulent Round Jet Subjected to Pulsed Vortex Generating Jets" ASME *Fluids Engineering Division Summer Meeting, High Speed Jet Flows Forum*. FED-Vol. 237, PP. 535-542, San Diego, CA

Parekh, D.E., Kibeus V, Glezer, A., Wiltze, J.M., and Smith, 1996, "Innovative Jet Flow Control: Mixing Enhancement Experiments, " AIAA 96-0308.

Sighal, A. K. "Key elements of verification and validation of CFD software" *AIAA98-2639, 29th AIAA, Fluid dynamic conference*, Allbuqurqe, NM, June 15-18, 1998.

Raman G. and Cornelius D., 1995, "Jet Mixing Control Using Excitation From Miniature Oscillation Jets," *AIAA Journal,* Vol.33, No 2, pp 365-368.

Vandsburger, U and Ding, C., 1995, "The Spatial Modulation of a Forced Triangular Jet" *Journal Experiments in Flud.* Vol 18, PP 239-248.

Wiltse, J. M. and Glezer, A., 1993, "Manipulation of Free Sheer Flows Using Piezoelectric Actuators" *Journal Fluid Mechanic.* Vol. 249, pp 261-285.

Wittmer, K. S, Devenport, W. J. and Zsoldos, J. S., 1998, "A Four-sensor Hot Wire Probe System for Three-Component Velocity Measurement," *J. Experiment in Fluids,* Vol.24 pp.416-423.

Zaman, K. B. M. Q. a, Reader, M. F and Samimy, M., 1994, "Control of an Axisymmetric Jet Vortex Generators," *J. Phys. Fluid* Vol. 6, No. 2, pp. 778-793.

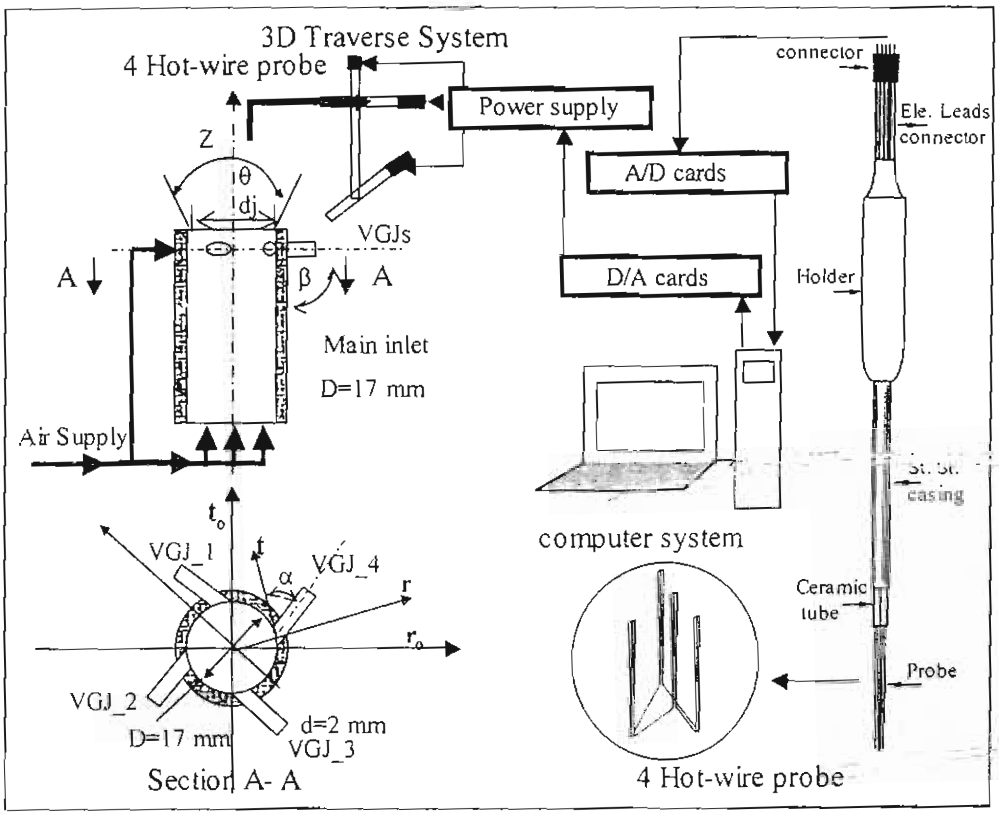

Fig. (1) Swirl jet construction and measuring instrumentation.

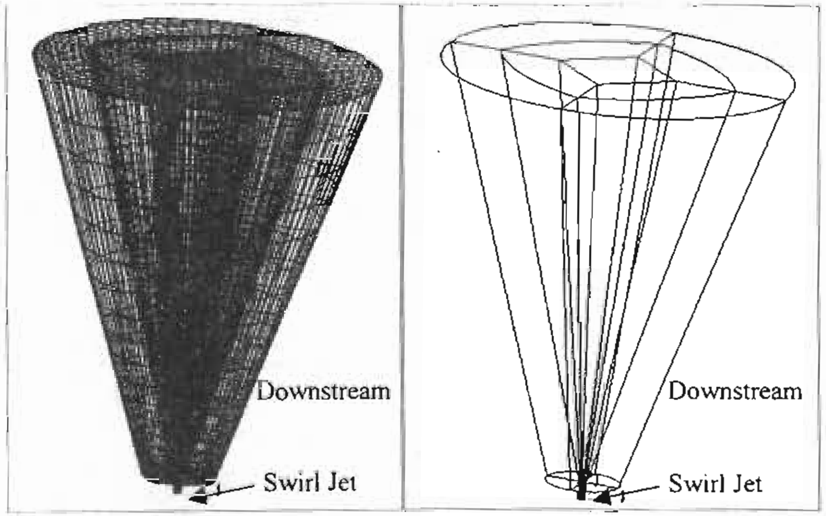

2.a) Grids over view. 2.b) Blocks downstream.

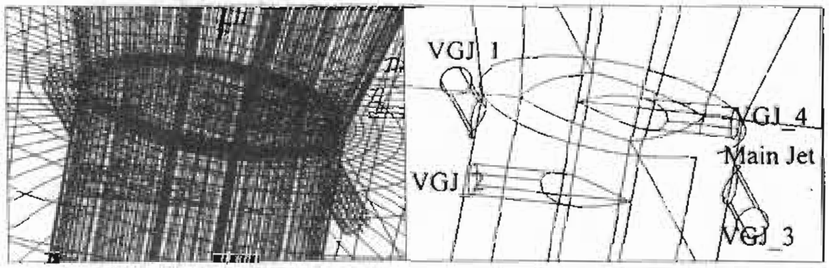

2.c) Arbitrary interfaces of VGJs and main jet. 2.d) Blocks at Swirl jet.

Fig. (2) 3D Grids in asymmetrical swirl jet and its downstream.

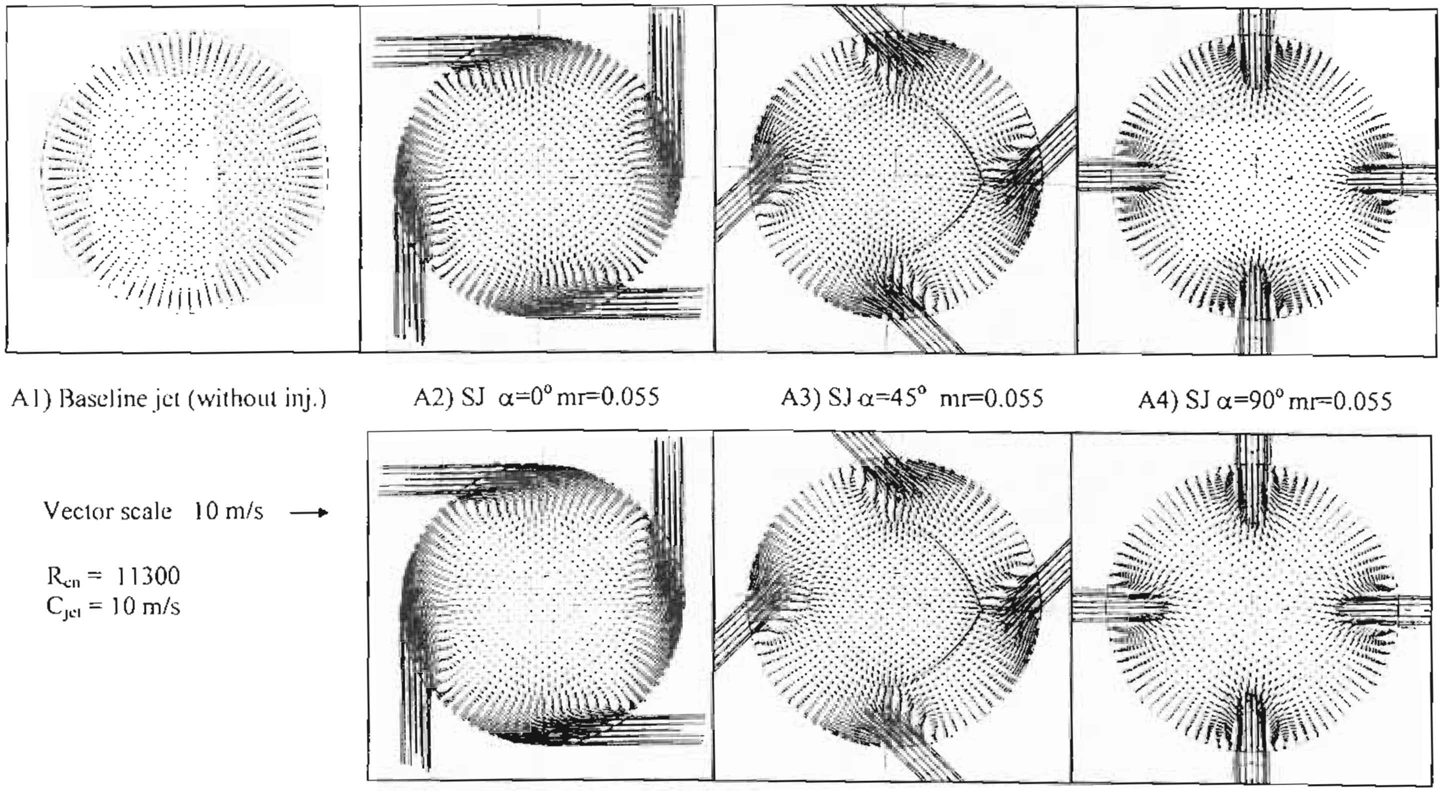

A1) Baseline jet (without inj.) A2) SJ α=0° mr=0.055 A3) SJ α=45° mr=0.055 A4) SJ α=90° mr=0.055

B1) SJ α=0° mr=0.078 B2) SJ. α=45° mr=0.078 B3) SJ α=90° mr=0.078

Fig. 3 Computational velocity vector projection at horizontal injection plane.

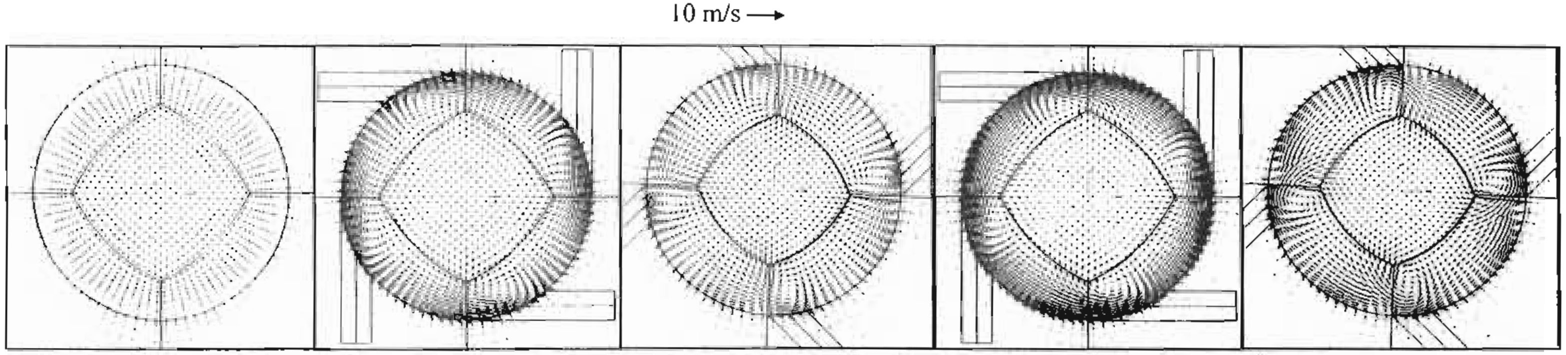

A1) Baseline jet (without inj.) A2) SJ α=0° mr=0.055 A3) SJ α=45° mr=0.055 A4) SJ α=0° mr=0.078 A5) SJ α=45° mr=0.078

Fig. 4 Computational velocity vector projection in horizontal planes just after jet exit from main jet.

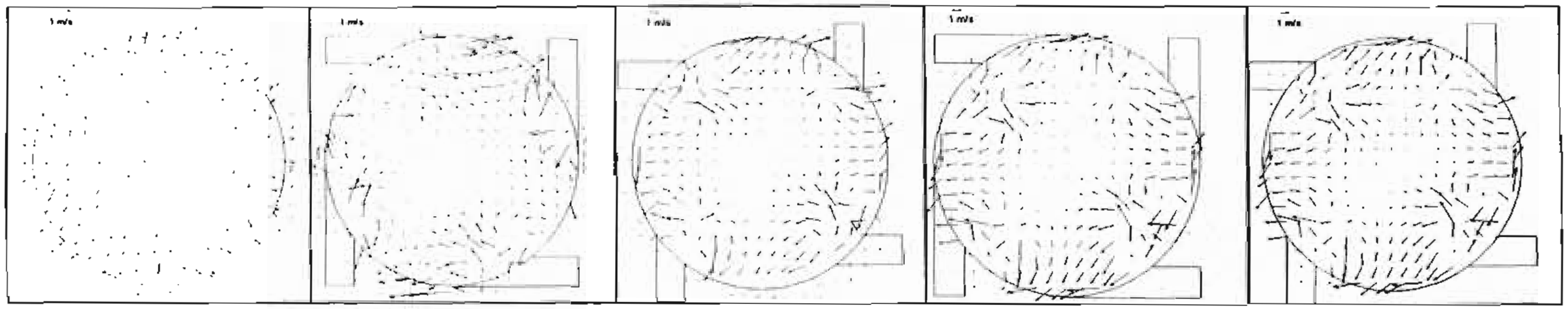

A1) Baseline jet (without inj.) A2) SJ α=0° mr=0.055 A3) SJ α=45° mr=0.055 A4) SJ α=0° mr=0.078 A5) SJ α=45° mr=0.078

Fig. 5 Experimental velocity vector projection i horizontal planes just after jet exit from main jet

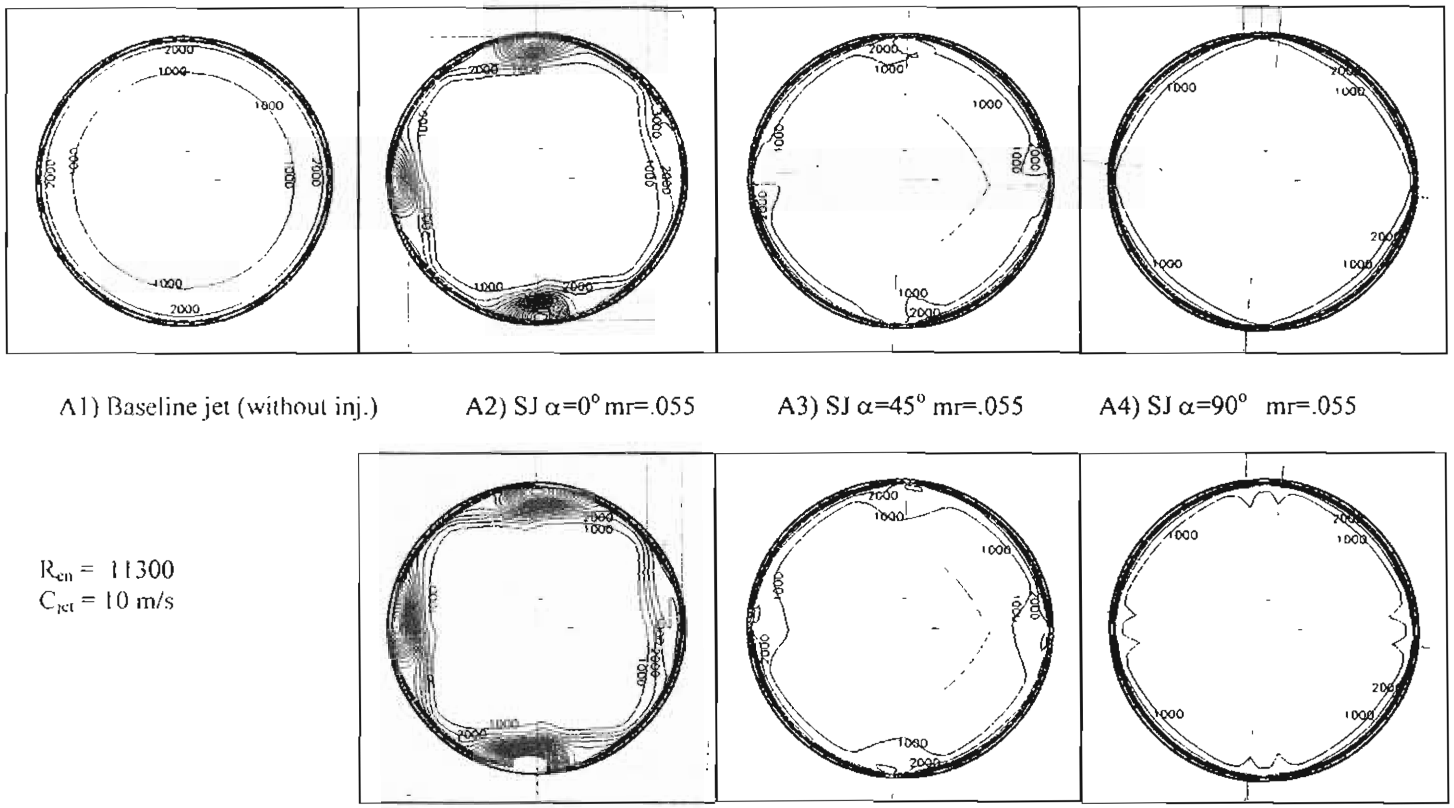

A1) Baseline jet (without inj.) A2) SJ $\alpha=0^\circ$ mr=.055 A3) SJ $\alpha=45^\circ$ mr=.055 A4) SJ $\alpha=90^\circ$ mr=.055

R_{en} = 11300
C_{jet} = 10 m/s

B1) SJ $\alpha=0^\circ$ mr=.078 B2) SJ $\alpha=45^\circ$ mr=.078 B3) SJ $\alpha=90^\circ$ mr=.078

Fig. 6 Computational iso-contour of turbulence dissipation rate (ε) (J/kg.s) for baseline jet and swirl jet at horizontal exit plane

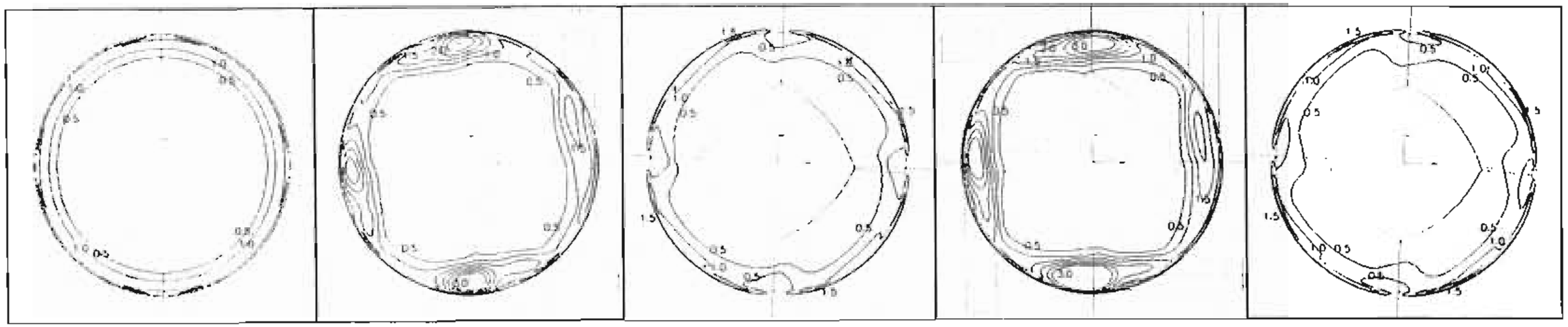

A1) Baseline jet (without inj.) A2) SJ α=0° mr=.055 A3) SJ α=45° mr=.055 A4) SJ α=0° mr=.078 A5) SJ α=45° mr=.078

Fig. 7 Computational iso-contour of turbulence kinetic energy (κ) for baseline jet and swirl jet at a horizontal plane. Z/D=0.

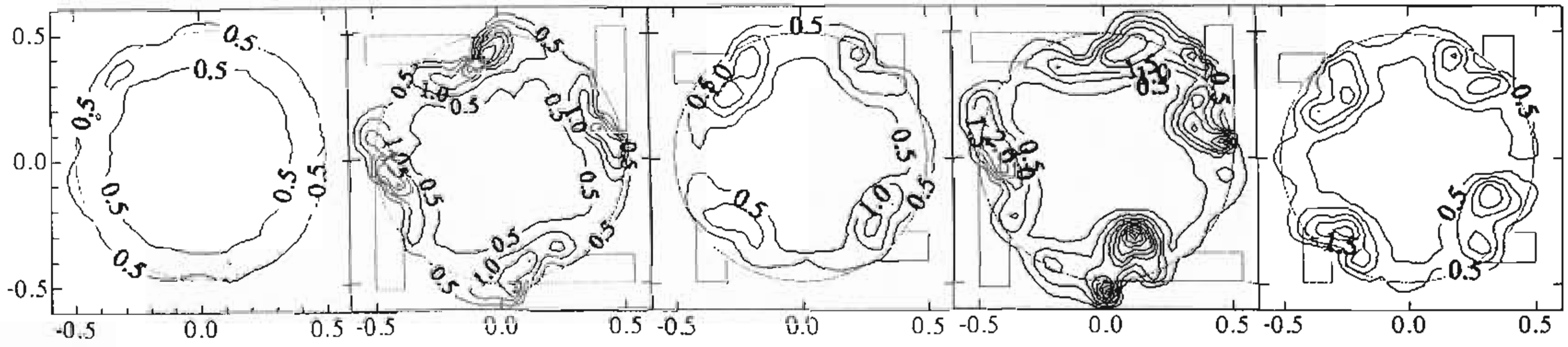

A1) Baseline jet (without inj.) A2) SJ α=0° mr=.055 A3) SJ α=45° mr=.055 A4) SJ α=0° mr=.078 A5) SJ α=45° mr=.078

Fig. 8 Experimental iso-contour of total turbulence kinetic energy $[(\overline{u}^2+\overline{v}^2+\overline{w}^2)/2]$, ($m^2/s^2$), for baseline jet and swirl jet at a horizontal plane. Z/D=0.

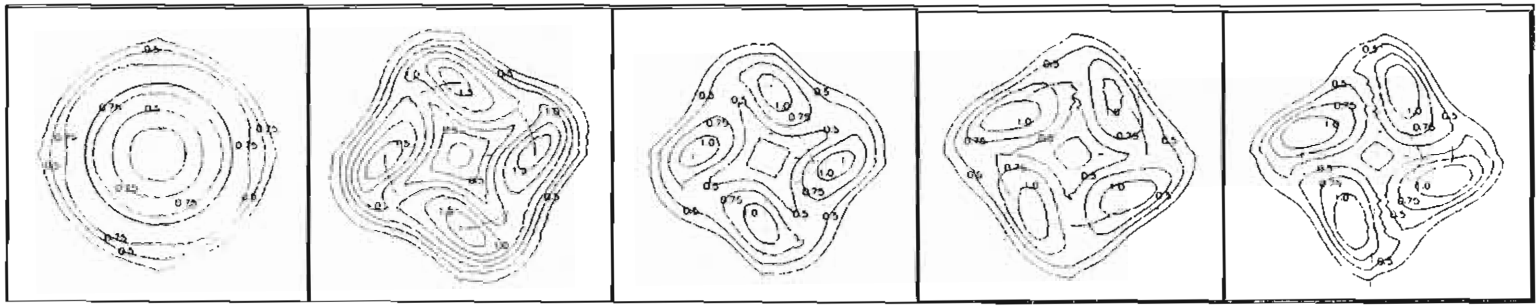

A1) Baseline jet (without inj.) A2) SJ α=0° mr=.055 A3) SJ α=45° mr=.055 A4) SJ α=0° mr=.078 A5) SJ α=45° mr=.078

Fig. 9 Computational iso-contour of turbulence kinetic energy (κ) for baseline jet and swirl jet at a horizontal plane. Z/D=3.

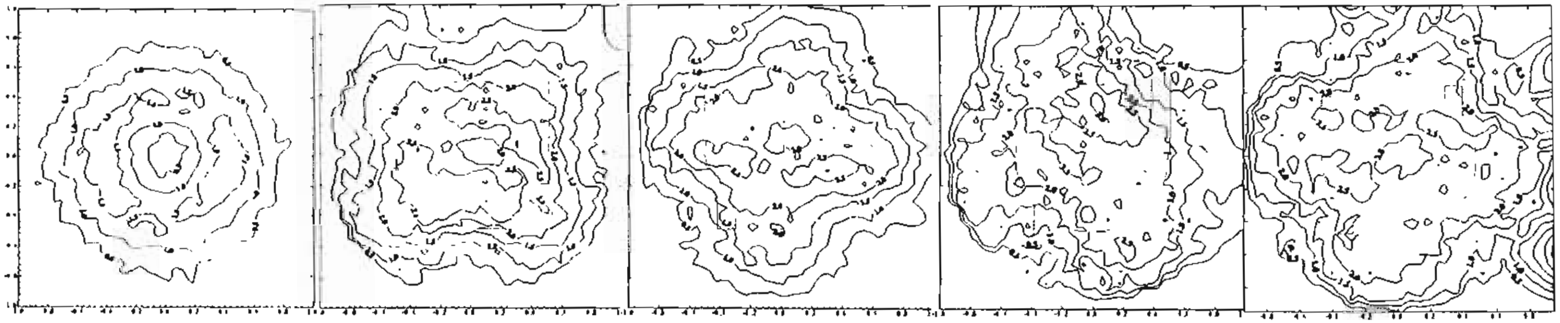

A1) Baseline jet (without inj.) A2) SJ α=0° mr=.055 A3) SJ α=45° mr=.055 A4) SJ α=0° mr=.078 A5) SJ α=45° mr=.078

Fig. 10 Experimental iso-contour of total turbulence kinetic energy $[(\overline{u}^2+\overline{v}^2+\overline{w}^2)/2]$, ($m^2/s^2$), for baseline jet and swirl jet at a horizontal plane.

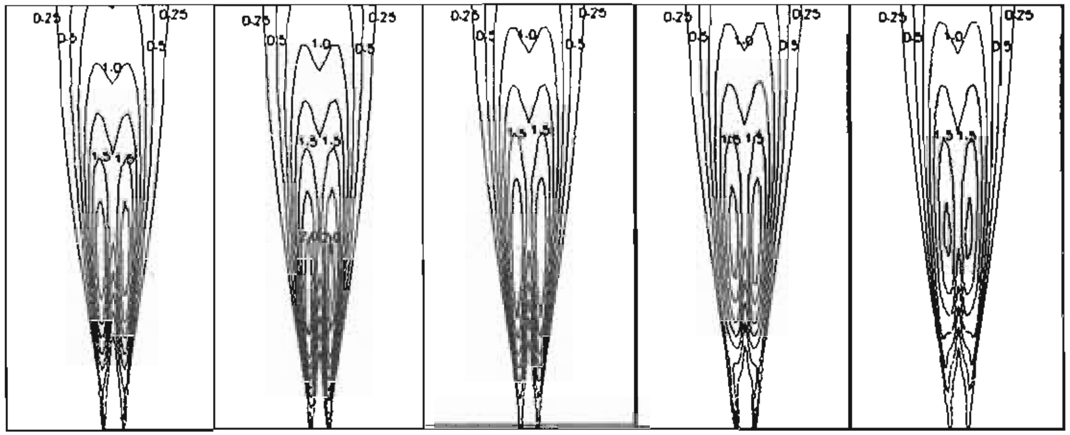

A1) Baseline jet A2) SJ α=0° mr=.055 A3) SJ α=45° mr=.055 A4) SJ α=0° mr=.078 A5) SJ α=45° mr=.078

Fig. 11 Computational iso-contour of turbulence kinetic energy (κ) for baseline jet and swirl jet at a vertical diametric plane.

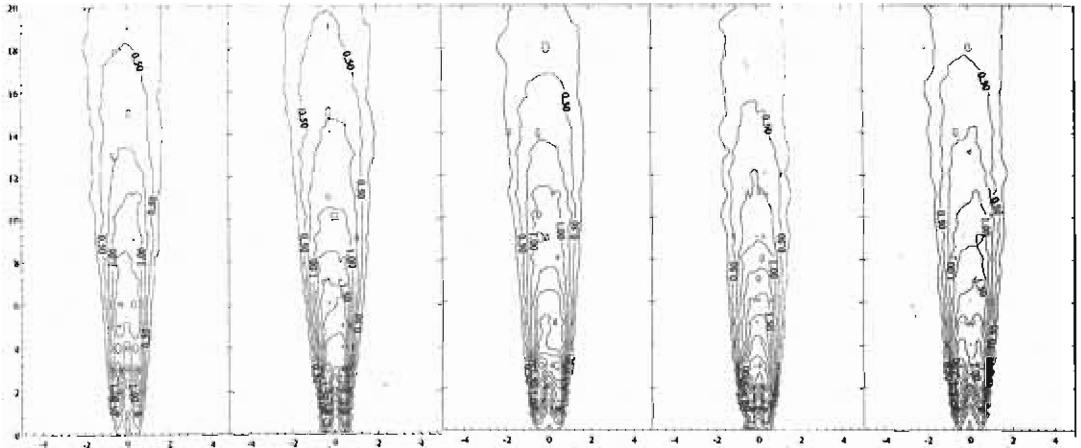

A1) Baseline jet A2) SJ α=0° mr=.055 A3) SJ α=45° mr=.055 A4) SJ α=0° mr=.078 A5) SJ α=45° mr=.078

Fig. 12 Experimental iso-contour of total turbulence kinetic energy $[(\overline{u}^2 + \overline{v}^2 + \overline{w}^2)/2]$, ($m^2/s^2$), for baseline jet and swirl jet

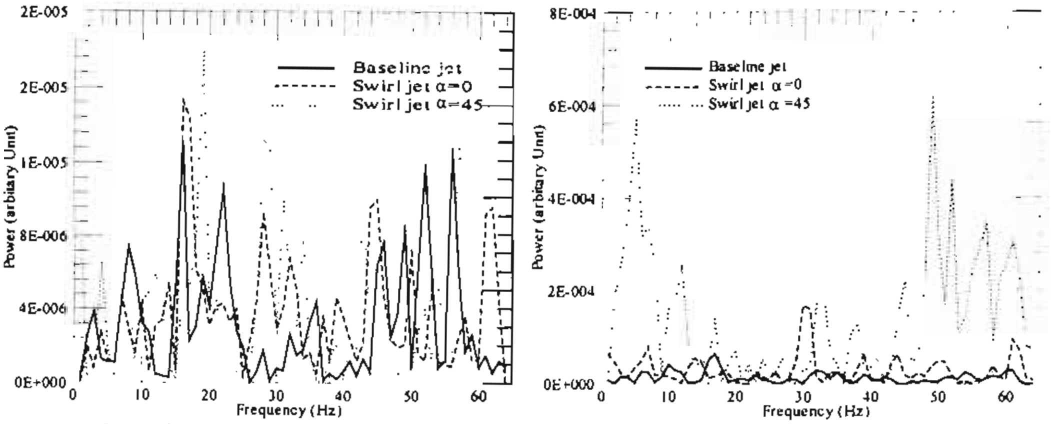

a) Velocity frequency spectrum at ($r_o/D=0$, $t_o/D=0$, $z/D=0$) b) Velocity frequency spectrum at ($r_o/D=0$, $t_o/D=0$, $z/D=3$)

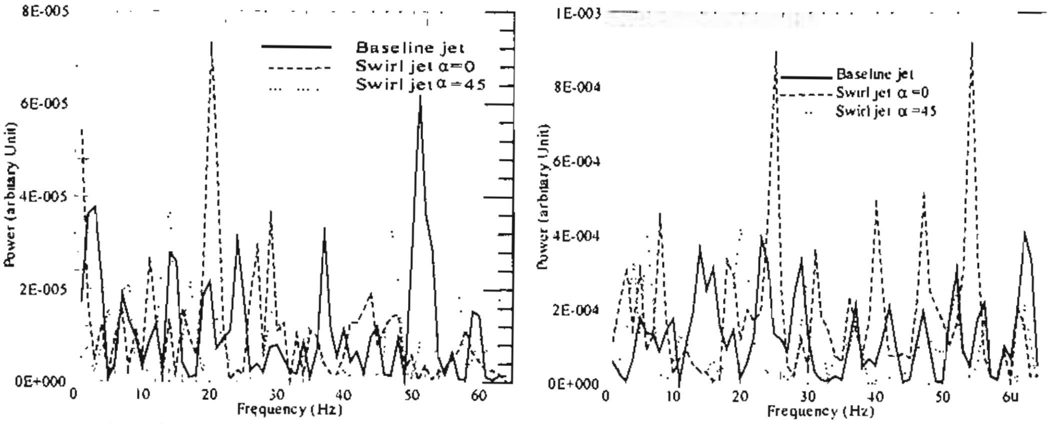

c) Velocity frequency spectrum at ($r_o/D=0.4$, $t_o/D=0$, $z/D=0$) d) Velocity frequency spectrum at ($r_o/D=0.4$, $t_o/D=0$, $z/D=3$)

Fig. 13 Velocity frequency spectrum for baseline jet and swirl jet at different levels.

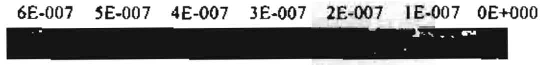

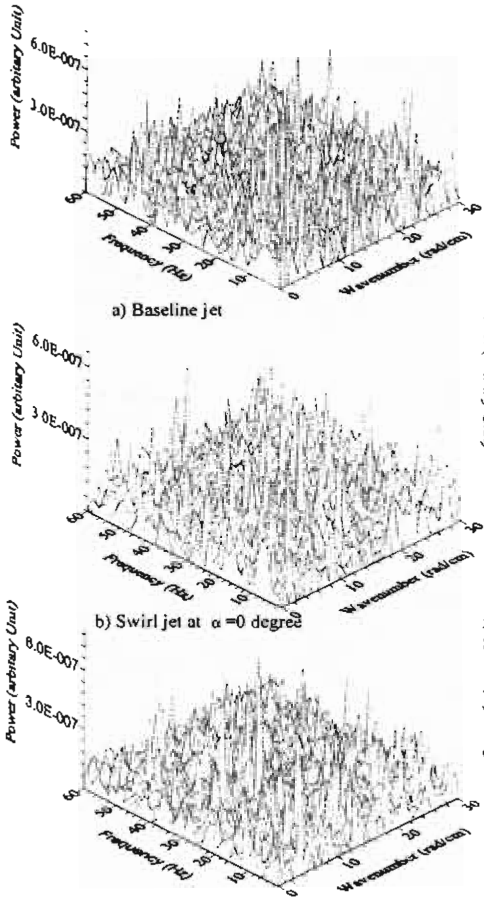

a) Baseline jet

b) Swirl jet at α =0 degree

c) Swirl jet at α =45 degree

Fig. 14 Wavenumber-frequency spectra of velocity fluctuation for different jets at ($r_o/D=0$, $t_o/D=0, z/D=0$).

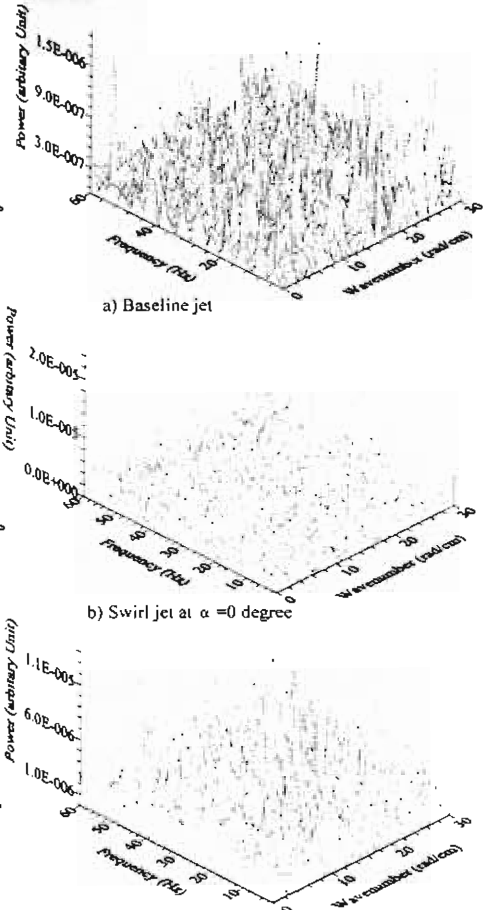

a) Baseline jet

b) Swirl jet at α =0 degree

c) Swirl jet at α =45 degree

Fig.15 Wavenumber-frequency spectra of velocity fluctuation for different jets at ($r_o/D=0$, $t_o/D=0, z/D=3$).

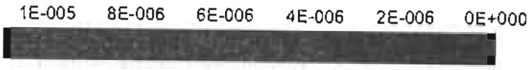

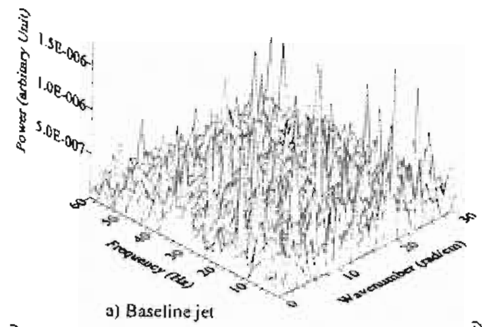

a) Baseline jet

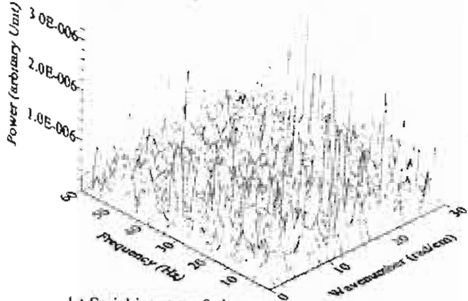

b) Swirl jet at α =0 degree

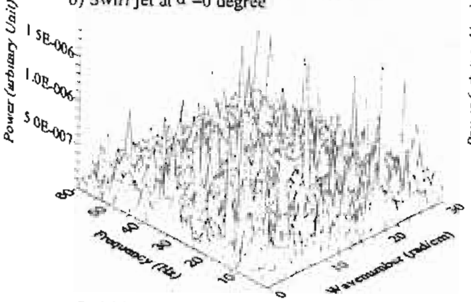

c) Swirl jet at α =45 degree

Fig. 16 Wavenumber-frequency spectra of velocity fluctuation for different jets at $(r_o/D=0.4, t_o/D=0, z/D=0)$.

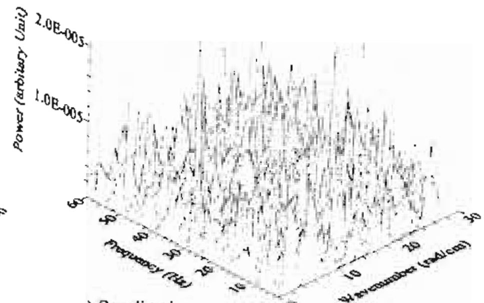

a) Baseline jet

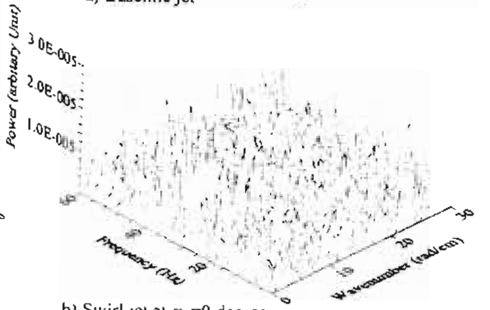

b) Swirl jet at α =0 degree

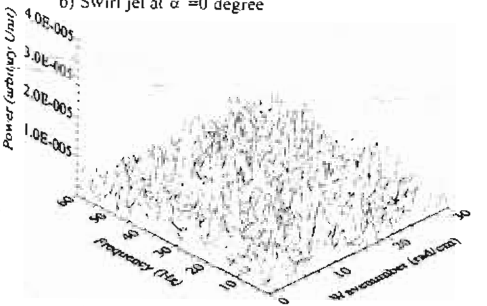

c) Swirl jet at α=45 degree

Fig.17 Wavenumber-frequency spectra of velocity fluctuation for different jets at $(r_o/D=0.4, t_o/D=0, z/D=3)$.

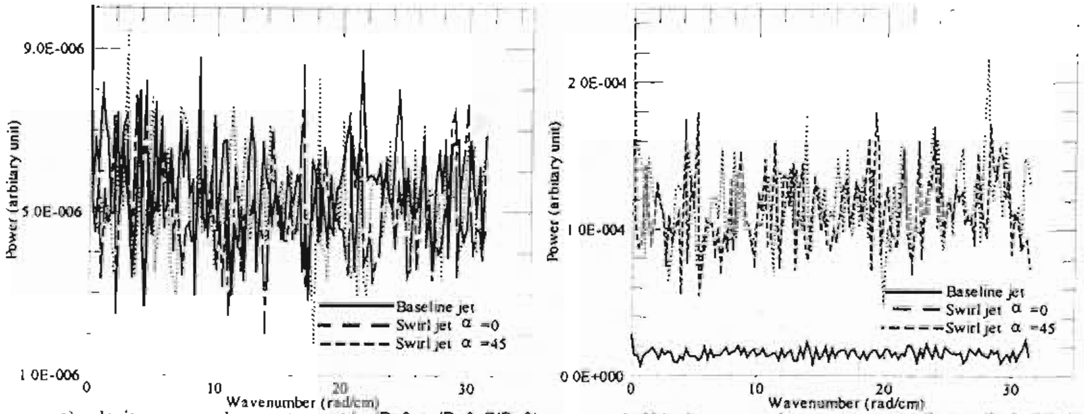

a) locity wavenumber spectrum at ($r_0/D=0$, $t_0/D=0$, $Z/D=0$) b) Velocity wavenumber spectrum at ($r_0/D=0$, $t_0/D=0$, $Z/D=3$)

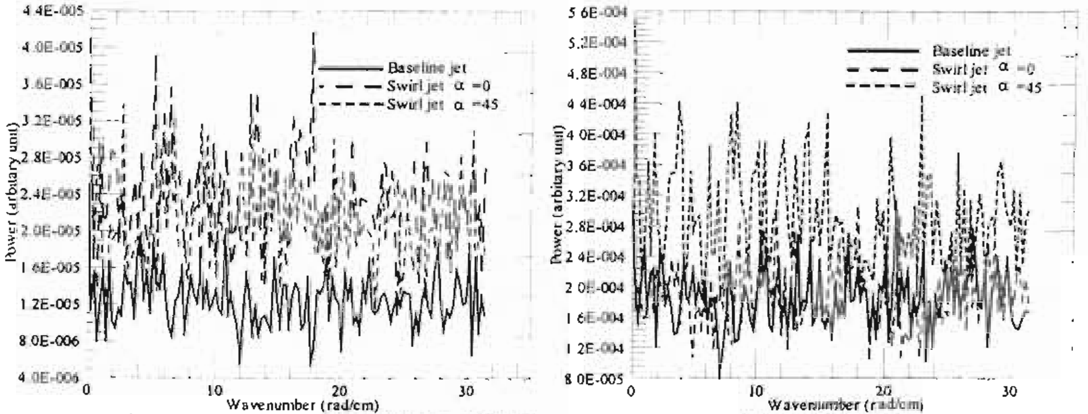

c) Velocity wavenumber spectrum at ($r_0/D=0.4$, $t_0/D=0$, $Z/D=0$) d) Velocity wavenumber spectrum at ($r_0/D=0.4$, $t_0/D=0$, $Z/D=3$)

Fig. 18 Velocity wavenumber spectrum for baseline jet and swirl jets at different levels.